*Nucleic Acids Research*, 2024, **52**, 8897–8912
https://doi.org/10.1093/nar/gkae574
Advance access publication date: 5 July 2024
**Genome integrity, repair and replication**

# Nuclear F-actin assembly on damaged chromatin is regulated by DYRK1A and Spir1 phosphorylation

**Junshi Li[1,2], Nan Xiong[1,2], Kirk L. West[3], Manton Leung[1], Yick Pang Ching[1], Jun Huang[4,5,6], Jian Yuan[7], Cheng-Han Yu[1,*], Justin Leung[8,*] and Michael Huen[1,2,*]**

[1]School of Biomedical Sciences, LKS Faculty of Medicine, The University of Hong Kong, Hong Kong, S.A.R.
[2]State Key Laboratory of Brain and Cognitive Sciences, The University of Hong Kong, Hong Kong, S.A.R.
[3]Department of Biochemistry and Molecular Biology, University of Arkansas for Medical Sciences, Little Rock, AR 72205, USA
[4]The MOE Key Laboratory of Biosystems Homeostasis & Protection, Life Sciences Institute, Zhejiang University, Hangzhou 310058, China
[5]Cancer Center, Zhejiang University, Hangzhou 310058, China
[6]Department of General Surgery, Sir Run Run Shaw Hospital, Zhejiang University School of Medicine, Hangzhou 310058, China
[7]Department of Biochemistry and Molecular Biology, Tongji University School of Medicine, Shanghai, China
[8]Department of Radiation Oncology, University of Texas Health Science Center at San Antonio, San Antonio, TX 78229, USA

[*]To whom correspondence should be addressed. Tel: +852 39176868; Fax: +852 28170857; Email: huen.michael@hku.hk
Correspondence may also be addressed to Justin Leung. Tel: +1 2105671204; Email: leungj@uthscsa.edu
Correspondence may also be addressed to Cheng-Han Yu. Tel: +852 39179205; Fax: +852 28170857; Email: chyu1@hku.hk

## Abstract

Nuclear actin-based movements support DNA double-strand break (DSB) repair. However, molecular determinants that promote filamentous actin (F-actin) formation on the damaged chromatin remain undefined. Here we describe the DYRK1A kinase as a nuclear activity that promotes local F-actin assembly to support DSB mobility and repair, accomplished in part by its targeting of actin nucleator spire homolog 1 (Spir1). Indeed, perturbing DYRK1A-dependent phosphorylation of S482 mis-regulated Spir1 accumulation at damaged-modified chromatin, and led to compromised DSB-associated actin polymerization and attenuated DNA repair. Our findings uncover a role of the DYRK1A–Spir1 axis in nuclear actin dynamics during early DSB responses, and highlight the intricate details of nuclear cytoskeletal network in DSB repair and genome stability maintenance.

## Graphical abstract

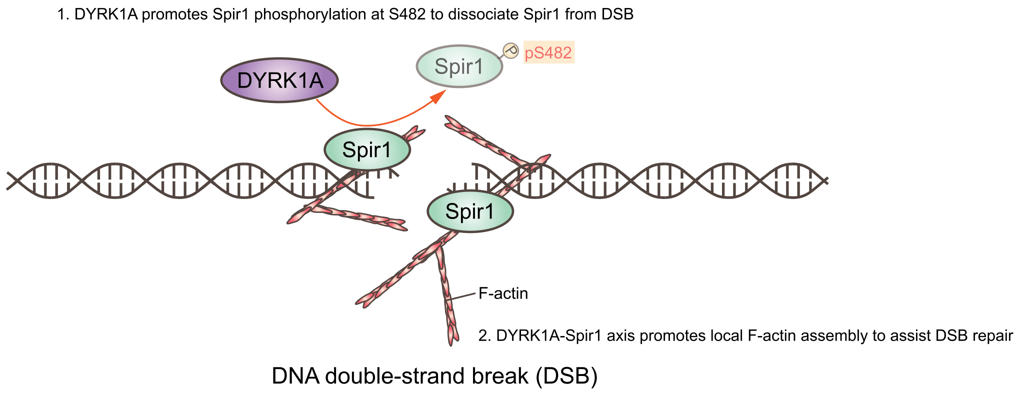

## Introduction

DNA double-strand breaks (DSBs) are one of the most cytotoxic lesions and require elaborated chromatin responses for effective repair (1,2). Notably, while chromatin is in constant motion within the cell nucleus, it has become established that mobility of the damaged chromatin increases (3–7) to drive DSB processing and repair (6,8,9). In addition to fostering homology search (3,8,10), DNA end resection (11), and suppression of aberrant recombination events (12,13), DSB mobilization also facilitates access of the damaged chromatin to DNA repair factors by relocalising DSBs outside of heterochromatin compartments (9,14), as well as by altering the dynamics of local chromatin condensation (15). Together, these seminal findings highlight DSB mobility as a driver for DNA repair,

**Received:** January 31, 2024. **Revised:** June 11, 2024. **Editorial Decision:** June 17, 2024. **Accepted:** June 20, 2024

encompassing both homology-dependent repair (HR) of DSBs as well as non-homologous end joining (NHEJ)-mediated repair of telomeric DNA (16,17).

To drive and direct DSB motions, cells rely on nuclear cytoskeletal network and an emerging list of regulatory factors (9,11,17,18). In particular, Spire proteins are endowed with actin nucleating activities and represent one of three major classes of actin nucleators (including Arp2/3 and formins) that promote actin polymerization (19,20). As one of the members in the Spire family, Spire homolog 1, hereafter referred to as Spir1, has been shown to interact with formin 2 (FMN2) to participate in actin filament elongation (20–22). Notably, loss of Spir1/2 proteins has been shown to compromise FMN2-mediated actin filament (F-actin) formation at DNA damage sites, implicating a role of Spir1/2 in controlling DSB-induced F-actin assembly (23). While nuclear actin filaments have been shown to assemble at sites of DNA damage to support Ataxia telangiectasia and Rad3 related (ATR) recruitment to DSBs and its downstream signaling events (24), the role of Spir1, together with the underlying mechanism(s) via which Spir1 regulates local F-actin organization at DSBs, remain to be defined.

Dual-specificity tyrosine phosphorylation-regulated kinase 1A (DYRK1A) is a serine/threonine kinase member of the DYRK protein kinase family (25). DYRK1A has documented functions in a variety of biological process that range from transcription to cell cycle progression (26–29). Notably, DYRK1A was previously identified as an interacting partner of the Ring Finger protein RNF169, a negative regulator of DSB signal transduction, suggesting that DYRK1A may also contribute to DSB repair control (30–32). In line with this idea, DYRK1A was more recently implicated in B cell class switch recombination by regulating MSH6 phosphorylation (33).

Here we report that the DYRK1A kinase mediates actin polymerization on the damaged chromatin via actin nucleator Spir1. We show that DYRK1A targets Spir1 at Ser482 to drive productive F-actin assembly and effective DSB repair. Our findings underscore pleotropic roles of the DYRK1A kinase in early DNA damage responses (DDRs).

## Materials and methods

### Cell culture

U2OS, HEK-293T and hTERT-RPE1 cells were cultured in DMEM supplemented with 10% fetal bovine serum (FBS) and 1% Pen-Strep at 37°C in 5% $CO_2$ with saturated humidity. U2OS-AID-DIvA cells, a kind gift from Dr G. Legube (CBI Toulouse), were cultured as described previously (34,35).

### Plasmids, primers, antibodies, chemicals and ionizing radiation

Antibodies, chemicals, and plasmids used in this study are listed in Supplementary Table S1. Primers used in this study are listed in Supplementary Table S2. Guide RNA (gRNA) sequences were cloned into LentiCRISPR-v2 plasmid backbone following the instruction of Target Guide Sequence Cloning Protocol (Gecko) (36,37). Unless specified otherwise, cDNAs were transferred to their respective expression vectors by Gateway cloning (Invitrogen). Ionizing radiation (IR) was delivered using the Gammacell® 3000 Elan irradiator according to manufacturer instructions.

### Transient transfection and RNA interference

For transient transfection of plasmids, plasmids were mixed with polyethylenimine (PEI) with a mass ratio of 1:4 in serum-free DMEM. The transfection mix was incubated at room temperature for 15 min and were applied to cells. Cells were harvested 24 hours after transfection for experiments. For knockdown experiments using small interfering RNA (siRNA), siRNA was mixed with Oligofectamine (Invitrogen) in serum-free DMEM, followed by incubation at room temperature for 15 min. Cells were washed once with 1× PBS, followed by incubation with siRNA mix for 8 h. FBS-containing culture medium was subsequently added to the transfected cells. Cells were transfected with siRNA as described above for three rounds at 24 h intervals and were harvested at least 48 h after siRNA transfection for experiments.

### Lentiviral packaging and transduction

HEK293T cells were co-transfected with the target lentiviral-based construct, and packaging plasmids psPAX2 and pMD2.G at a mass ratio of 4:3:1 using PEI. Supernatant containing lentiviral particles were collected and filtered (0.45 μm) at 48 h and 72 h after transfection, respectively. For transduction, the filtered supernatant was mixed with polybrene (8.0 μg/ml) and were applied to the recipient cells. The recipient cells were transduced twice at 24-h intervals prior to antibiotic selection.

### Generation of knockout cell line using CRISPR/Cas9 system

Oligos of the guide RNA (gRNA) were cloned into plentiCRISPR-V2 vector as described (36). The constructs were then subjected to lentiviral packaging and transduction procedures described above, and transduced cells were thereafter selected by puromycin (2.0μg/ml). Knockout efficiency of cells was verified by western blotting analysis. To obtain clean knockout cell lines, the pool knockout cells were subcloned when necessary. The sequence of gRNAs used in this study are listed in Supplementary Table S2.

### Generation of doxycycline-inducible stable cell lines for ectopic protein expression

cDNAs were cloned into a lentiviral-based expression vector containing a Tet response element (TRE) promoter and an SFB (S protein, Flag, and Streptavidin-binding peptide)-expressing sequence. Expression constructs were delivered into target cells following lentiviral packaging and transduction procedures described above. The transduced cells were subsequently selected using G418 (2.0mg/ml) for one week. To induce ectopic protein expression, cells were incubated in doxycyclin (Dox; Sigma) at indicated concentrations for 24 h prior to experiments.

### Western blotting

Cells scraped from culture dishes were pelleted at 5000 rpm, followed by lysis using NETN buffer (20 mM Tris–HCl, pH 8.0, 100 mM NaCl, 0.5% NP40 substitute and 1 mM EDTA) supplemented with Bitnuclease (Biotool) on ice for 20 min. 10 mM β-glycerol phosphate was added to the lysis buffer when necessary. The lysates were then mixed with 4× SDS loading buffer and boiled for 5 min. Proteins in boiled lysates were separated by SDS-PAGE and transferred to

PVDF membranes. The membranes were subsequently blotted with indicated primary antibodies. Protein bands were visualized by the ChemiDoc™ MP imaging system (Bio-Rad) after the addition of SuperSignal® West Pico Chemiluminescent Substrate (Thermo Scientific) onto the blotted membranes.

## Subcellular fractionation to obtain nuclear-enriched extract

HEK293T cells from one 10cm dish were harvested and resuspended in 400 μl ice-cold fractionation buffer A (10 mM HEPES, pH7 .9, 10 mM KCl, 1.5 mM $MgCl_2$, 0.5 mM DTT), followed by incubation on ice for 5 min. Crude nuclear extract was obtained from this cell suspension via centrifugation at 250 rcf for 5 min at 4°C, followed by aspiration of supernatant. This crude nuclear extract was resuspended in 200μl chilled buffer S1 (0.25M sucrose, 10mM $MgCl_2$) and layered on 200 μl chilled buffer S2 (0.35 M sucrose, 0.5 mM $MgCl_2$). The crude nuclear extract was then further purified via centrifugation at 1450 rcf for 5 min at 4°C, followed by supernatant removal. The pellet containing nuclear-enriched extract was washed by ice-cold NETN buffer for downstream experiment(s).

## Coimmunoprecipitation (co-IP) and denaturing immunoprecipitation

For co-IP experiments, cells were pelleted and lysed with 200μl NETN buffer supplemented with Bitnuclease (Biotool) on ice for 20 min and topped up with 600 μl chilled NETN buffer thereafter. Clear supernatant was collected from the lysate by a centrifugation at 15 000 rpm at 4°C for 10 min, followed by the incubation with Streptavidin beads (GE Healthcare) on rocker at 4°C for 4 h. The beads were then washed with chilled NETN buffer, boiled with SDS loading buffer and subjected to Western blotting analysis. For denaturing immunoprecipitation, cell pellets were lysed using NETN buffer supplemented with Bitnuclease (Biotool) and β on ice for 20 min and topped up by 600 μl chilled denaturing buffer (20 mM Tris–HCl, pH 8.0, 50 mM NaCl, 0.5% NP40, 0.5% deoxycholate, 1% SDS and 1 mM EDTA). The lysates were then boiled for 5 min and centrifuged at 15 000 rpm at 4°C for 10 min. Clear supernatant was collected and incubated with anti-Flag resin (Biotool) on rocker at 4°C overnight. After incubation, the beads were washed with chilled denaturing buffer, boiled with SDS loading buffer and were proceeded for SDS-PAGE analysis.

## Immunofluorescence (IF) staining

A monolayer of cells grown on cover slips were fixed using 3% paraformaldehyde (PFA) at room temperature for 15 min, followed by permeabilization using 0.5% triton solution for 10 s. Permeabilized cells were sequentially incubated with indicated primary antibodies for 45 min at room temperature, followed by fluorophore-conjugated secondary antibodies for 45 min at room temperature. The antibodies were diluted in 3% BSA solution. Nuclei were stained using DAPI diluted in 1× PBS. The stained coverslips were mounted on glass slides with mounting medium (Dako, Agilent). Images were captured using an Olympus BX53 fluorescence microscope for analysis in ImageJ.

## Laser microirradiation experiments

U2OS cells cultured on glass-bottomed 35 mm confocal dishes (SPL Life Sciences) were transfected with the indicated GFP-tagged expression constructs. The confocal dishes were placed into a 37°C live cell chamber supplied with 5% $CO_2$ for laser microirradiation 24 h after transfection. Laser microirradiation was conducted on a Zeiss LSM 780 Inverted Confocal Microscope equipped with Coherent Chameleon Vision Laser II. The laser output for inducing localized DNA damage was set to be 750 nm (11% power) with two-photon processing. Timelapse images were acquired using ZEN 2012 software (Carl Zeiss) and a 40 × 1.4 oil DIC objective. Fading of emission intensity over time in the timelapse images collected were corrected using the bleach correction function in Fiji. Intensity of the microirradiated ROI over time in bleach-corrected images was measured using Fiji. The timepoint before microirradiation was set as t=-2s, while the timepoint immediately after microirradiation was set as $t = 0$ s. The ROI intensity at t = 0s was used as the background value. Normalized intensity was calculated following the equation below:

$$\text{Normalised intensity} = \frac{\text{MFI of microirradiated ROI at t} = \text{ns} - \text{MFI of microirradiated ROI at t} = 0\text{s}}{\text{MFI of microirradiated ROI at t} = -2\text{s} - \text{MFI of microirradiated ROI at t} = 0\text{s}}$$

where MFI stands for mean fluorescence intensity. For statistical testing, traces of normalized intensity values over time were fitted to one-phase association model using the nonlinear regression function in GraphPad Prism 8 software (Dotmatics). Individual span values, in this case the plateau of each fitted curve, were plotted for statistical analysis, and are shown as individual datapoints in the bar charts. Unless stated otherwise, all microirradiation data in this study was collected from 3 independent experiments.

For microirradiation experiments in cells for immunofluorescence (IF) staining, a monolayer of U2OS cells were grown on Φ25mm round cover slips (Epredia). The cover slips with cells were secured with Attofluor™ Cell Chamber (Invitrogen). During microirradiation, this chamber was incubated at 37°C with 5% $CO_2$ and saturated humidity. DNA damage was induced by 750 nm two-photon laser mentioned above, with an output power of 80%. This laser light was applied to the cover slip under a 10× objective, with a 4 × 5 tile scan and a line strep of 8. These microirradiated cells on cover slips were fixed using 3% PFA as described above for IF staining.

## Metaphase spreading

After 3Gy radiation, hTERT-RPE1 cells were incubated in culture medium with 0.03μg/ml colcemid (GibcoTMKaryoMAXTM) for 3 h at 37°C. Cells were subsequently harvested and incubated in 2ml 0.8% (m/v) sodium citrate for 15 min at 37°C, followed by the addition of 5ml freshly prepared fixative (methanol: acetic acid, 3:1, v/v) and further incubation for 5 min at 37°C. Cells were thereafter washed with the fixative for three times and resuspended in up to 0.5 ml fixative. 20 μl of suspension was dropped onto clean glass slides and air-dried. To visualize metaphases, the air-dried glass slides were stained with DAPI solution, mounted with coverslips, and observed under 100× oil immersion lens of Nikon fluorescence microscope for quantifying chromosomal aberrations.

## G2/M checkpoint assay

Cells were trypsinized and harvested at indicated timepoints after 3Gy IR challenge. Harvested cells were washed once with ice-cold 1xPBS, followed by fixation using ice-cold 70% ethanol added in a dropwise manner. After overnight incubation at –20°C, cells were washed once with 1× PBS. Mitotic cells were labeled by sequential incubation in anti-H3pSer10 antibody, followed by the corresponding FTIC-conjugated secondary antibody. Each antibody was diluted in 200 μl 50mM sodium citrate for a 30-minute incubation with cells at room temperature. Cells were washed twice with 1× PBS after each antibody incubation. The stained cells were subjected to RNase A digestion in 50mM sodium citrate for 30 min at room temperature, followed by the addition of propidium iodide (50μg/ml). The mitotic population labeled was visualized by flow cytometric analysis using BD FACS CantoII Analyzer (San Jose, CA, USA).

## Live cell imaging of DSB foci tracking experiments

cDNAs of 53BP1 and PALB2 in Gateway-compatible entry vectors were transferred to lentiviral-based destination vector pLVpuro-CMV-N-mCherry. The resulting pLVpuro-CMV-mCherry-53BP1 and pLVpuro-CMV-mCherry-PALB2 were used for generating stable U2OS-DIvA cell lines with stable expression of mCherry-53BP1 and mCherry-PALB2, respectively, via lentiviral induction. These cell lines were cultured on glass-bottomed 35 mm confocal dishes (SPL Life Sciences). On the day of live cell imaging, cells were incubated with 600 nM 4-OHT for 4 h at 37°C. Cells were then washed with 1xPBS twice and were incubated with culture medium containing 500μg/ml auxin, together with DMSO or 100 μM CK-666 (Sigma Aldrich), respectively, for 1 h prior to imaging. Images were acquired using an Eclipse Ti2-E widefield microscope (Nikon) equipped with a 60× DIC N2 oil objective and a Tokai Hit on-stage incubation system. The Perfect Focus System (Nikon) was applied to maintain the focus throughout live cell imaging experiment. By using the Metamorph 7.10.2.240 software, images were collected as z-series at 0.4 μm-step were collected every 5 min for at least 45 min.

## Analysis of DSB foci mobility

Live cell images collected were processed using Fiji with the required plugins as described (38). Maximal intensity projections of each z-stack images were generated. These projections were grouped and imported as image series to construct t-stacks. As mCherry-tagged 53BP1 and PALB2 labeled the cell nucleus, the entire nuclear mCherry signal in the t-stacks was used for registration and drift correction using MultistackReg plugin. The TrackMate plugin were then applied to track foci movements during the imaging duration. Mean-square displacement (MSD) of these foci were calculated using the MSDanalyzer developed by Tarantino *et al.* (39) on the MATLAB (version R2022a) software. To calculate diffusion coefficient ($D$) and anomalous diffusion coefficient ($\alpha$), eight time intervals of the mean MSD curve of individual nucleus were fitted to the power law $\mathrm{MSD} = 4D(t)^{\alpha}$, where $t$ refers to time, using the Solver Add-in of Microsoft Excel. For DSB foci clustering analysis, a DSB foci cluster event is defined as at least two foci colocalise for at least three consecutive timeframes in the time-series images.

## TMTpro-16 labeling and phosphopeptides analysis

RPE-1, RPE-1 DYRK1A KO, RPE-1 TRE-DYRK1A(WT)-SFB and RPE1-TRE-DYRK1A(K188R)-SFB were cultured in the presence of 2 μg/ml doxycycline for 36 h prior to harvesting. Cells were lysed in 2% SDS and 100 mM Tris–HCl, pH 7.6 supplemented with fresh protease (Pierce, A32963) and phosphatase inhibitors (Pierce, A32957). Protein concentration was measured using BCA protein assay (Pierce, 23225) and 300 μg of protein were reduced with 5mM Tris(2-caboxyethyl) phosphine hydrochloride for 30 min at 37°C followed by alkylation using iodoacetamide (10mM, 30 min at room temperature), and purified via chloroform/methanol extraction. Protein pellets were digested with trypsin at a protein:trypsin ratio of 50:1 overnight at 37°C. Tryptic peptides were acidified with 0.1% formic acid and desalted on a C18 Sep-Pak (Waters, WAT054955). Eluted peptides were dried using SpeedVac. Four 300 μg replicates from each group were labeled using TMTproTM 16 plex labels (Thermo, A44521) following the manufacturer's instructions. 10 μl of labeled peptide from each sample was combined and analysed for proper mixing by mass spectrometry. After the ratio-check, labeled peptides were mixed in equal proportions and TMT-labeled phosphopeptides were enriched by TiO2 beads (High-Select TiO2 Phosphopeptide Enrichment Kit; Pierce, 88303) followed by the High-Select Fe-NTA Phosphopeptide Enrichment Kit (Pierce, A32992). Eluates from both kits were dried, resuspended and combined in basic buffer A (10mM ammonium hydroxide, pH 10). Combined eluates were fractionated in 42 fractions by basic pH reverse phase UltiMate 3000 ultra-high performance liquid chromatography system equipped with a 100× 1.0-mm Acquity BEH C18 column and a 40-min gradient from 99:1 to 60:40 basic buffer A:B ratio (basic buffer A: 0.1% formic acid, 0.5% acetonitrile, 10 mM ammonium hydroxide, pH 10; basic buffer B: 99.9% acetonitrile, 10 mM ammonium hydroxide, pH 10). TMT-labeled phosphopeptides were analysed as previously reported with the following changes (40). Fractionation was performed using an UltiMate 3000 RSLCnano equipped with a 150× 0.075-mm column packed with XSelect CSH C18 2.5 μM resin (Waters, 186006103) for reverse-phase fractionation, in-line with an Orbitrap Fusion Eclipse Tribrid mass spectrometer. Peptides were eluted over a 100-min gradient of 97:3 buffer A (0.1% formic and 0.5% acetonitrile) to buffer B (0.1% formic acid and 99.9% acetonitrile) to 67:33 A:B. Eluted peptides were ionized by electrospray ionization at 2.2 kV. TMTpro reporter quantities and peptide sequences were collected by Multinotch MS3 (41). Mass spectra (MS1) of 400–1600 $m/z$ was collected in the Orbitrap at 120 000 resolution. Higher-energy collisional dissociation (HCD) at 30.0 normalized collision energy was used to fragment selected ions and 200–1400 $m/z$ fragment ions were measured for second round mass spectrometry (MS2) in the ion trap. Synchronous precursor selection was employed to target up to 10 MS2 ions for fragmentation by HCD at 50.0 normalized collision energy and third round mass spectrometry (MS3) data were collected for reporter ions between 100 and 500 $m/z$ with 50000 resolution within the Orbitrap. Data were analysed using MaxQuant as previously described (40) with TMT-proTM 16-plex labeling for lysine residues and peptide N-termini as fixed modifications. Intensities corresponding to TMT-labeled, phosphopeptides were analysed in R using the Limma package.

### Pathway and process enrichment analysis

Gene ontology analysis and Network plots were generated using Metascape web-based portal (https://metascape.org/gp/index.html#/main/step1) (42). The following ontology databases were used for the pathway and process enrichment analysis: KEGG Pathway, GO Biological Processes, Reactome Gene Sets, Canonical Pathways, CORUM, WikiPathways and PANTHER Pathways. All genes in human genome were used as background for comparison. Ontology terms with *P*-values $<0.01$, minimum counts of 3, and enrichment factors $>1.5$ (the ratio of the observed count to the counts expected by chance) were grouped into clusters according to their similarities. In each cluster, the ontology term with the smallest *P*-value was selected as the representative of the cluster. For network plots, enriched terms, which were denoted by nodes, with Kappa similarities $>0.3$ were linked with edges.

### Statistical analysis

Error bars represent mean ± SEM from three independent experiments unless stated otherwise. When necessary, one-way ANOVA was performed for comparison of three of more groups prior to post-hoc t-tests. Two-tailed Student's $t$ test was performed for comparisons between two groups and a *P*-value $\leq 0.05$ would be considered as statistically significant.

## Results

### DYRK1A is recruited to DSBs

We first examined if DYRK1A may respond to laser-induced DNA damage using commercially available DYRK1A antibodies (Supplementary Figure S1A-B). Consistent with the idea that DYRK1A participates in DSB responses, we observed that laser microirradiation led to accumulation of DYRK1A protein at DNA damage tracks (Figure 1A–C). Moreover, DYRK1A also accumulates at FokI-induced DSBs (Supplementary Figure S1C). To probe how DYRK1A assembles at DSBs, we generated a panel of green fluorescence protein (GFP)-tagged DYRK1A alleles and examined their abilities to accumulate at laser-microirradiated sites (Figure 1D). Accordingly, we found that the DYRK1A N-terminus, which contains both the nuclear localisation sequence (NLS) and the RNF169-binding site (30), was required for productive accumulation of DYRK1A at DSBs (Figure 1E, F). Given the previously proposed RNF169-dependent role of DYRK1A in DSB repair (30–32), we therefore tested if the RNF169-DYRK1A interaction may be crucial for DYRK1A docking on laser-damaged DNA by examining RNF169-binding defective DYRK1A mutants (Figure 1G). Intriguingly, deletion of RNF169-binding sequence did not noticeably affect DYRK1A recruitment to laser-induced DSBs (Figure 1H, I), suggesting that the DYRK1A kinase may have RNF169-independent role(s) during early DSB responses.

To define the genetic requirements that license DYRK1A enrichment at DSBs, we chemically inhibited the activities of two master DNA Damage Response (DDR) regulators, namely Poly (ADP-ribose) polymerase (PARP) and Ataxia Telangiectasia Mutated (ATM). While ATM inhibition had minimal impact on DYRK1A docking at DSBs, DYRK1A accumulation at laser-induced DNA damage tracks was suppressed in PARP-inhibited cells (Figure 1J, K). These observations indicate that DYRK1A is a DSB-responsive factor, and that it may rely on PARP activities during early DDRs.

### DYRK1A promotes DSB repair

Consistent with a role of DYRK1A in DSB responses, DYRK1A depletion led to persistent IR-induced DNA damage foci, including those marked by DNA damage markers 53BP1 and γH2AX (Supplementary Figure S2A–C). Timely resolution of DNA damage foci strictly required its kinase activity, as wildtype (WT) but not its catalytic inactive K188R mutant complemented loss of DYRK1A (Supplementary Figure S2A–C). We also depleted DYRK1A in cells and examined their chromosomal stability following an ionizing radiation (IR) challenge. Chromosomal stability was analysed by scoring for chromosomal aberrations in metaphase cells after IR treatment. Accordingly, we found that DYRK1A-ablated cells displayed higher radiosensitivity when compared to control (Supplementary Figure S2D-F), in line with a recent study that reported a role of DYRK1A in conferring radioresistance in pancreatic cancer cells (43). Furthermore, such increase of radiosensitivity was rescued by WT DYRK1A but not its K188R mutant, indicating that the DYRK1A kinase activity is required to support chromosomal repair (Supplementary Figure S2D-F).

To exclude the possibility that elevated chromosomal aberrations detected in mitotic cells may have resulted from compromised G2 checkpoint arrest, we also examined if DYRK1A may be important for IR-induced G2/M checkpoint control. By monitoring cell entrance into mitosis, we found that DYRK1A was dispensable for G2/M checkpoint activation upon IR challenge (Supplementary Figure S3A–C). Taken together, our findings support the idea the DYRK1A kinase may play direct roles in DSB repair processes.

### Phospho-proteomic studies link DYRK1A to actin organization control

Given the requirement of the DYRK1A kinase activity in DSB repair, we profiled the DYRK1A phospho-proteome by comparing phospho-peptides from isogenic hTERT-RPE1 cell line derivatives, including parental cells, cells with ectopic Flag-tagged wildtype (WT-OE) and K188R (Mut-OE) DYRK1A expression, and DYRK1A knockout (KO) cells (Supplementary Figure S4A). Phospho-peptides significantly enriched in OE cells over the KO counterparts were considered putative DYRK1A targets (Supplementary Figure S4B, Supplementary Table S3). In line with the literature (44), motif analysis of putative DYRK1A substrates revealed that DYRK1A preferentially targeted serine/threonine (S/T) residues followed by a proline (P) residue, with an enrichment of arginine (R) residues at position -3 (Figure 2A). We also performed gene ontology analysis using Metascape web-based portal (42), and found that putative DYRK1A targets revealed strong association with actin organization control (Figure 2B-D). Although DYRK1A has been reported to negatively regulate actin polymerization in the cytoplasm (45–47), this prompted us to consider the possibility that DYRK1A may contribute to DSB repair by controlling nuclear actin dynamics.

### DYRK1A promotes F-actin assembly at DSBs and DSB mobility

To visualize nuclear actin dynamics at DSBs, we compared established subcellular localisation of F-actin probes, namely utrophin230-EGFP-3xNLS (Utr230-EN) and actin chromobody (Actin-CB-GFP-NLS) (Supplementary Figure S5A, B),

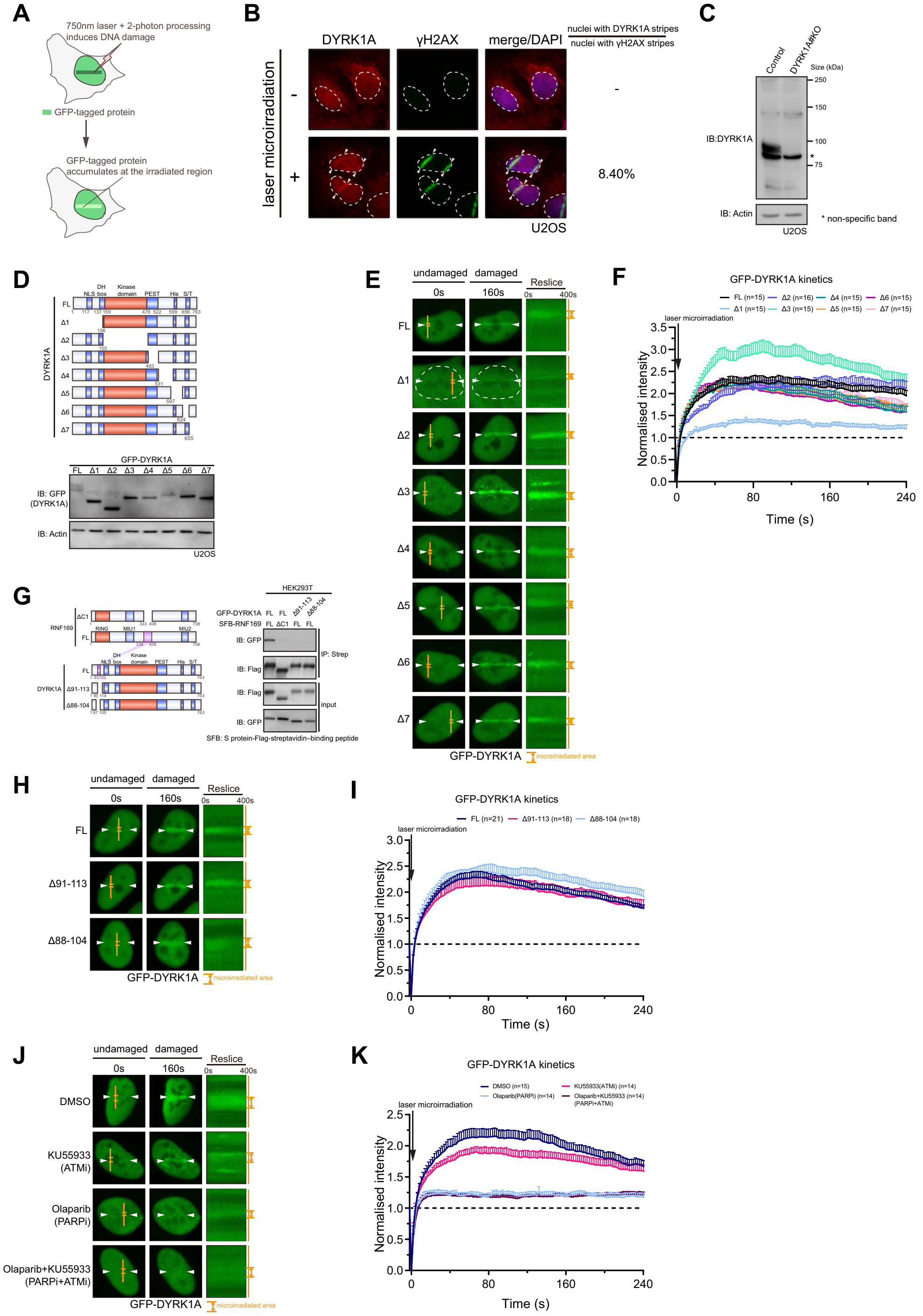

**Figure 1.** Early recruitment of DYRK1A requires PARP and is independent of binding to RNF169. (**A**) Schematic illustration of laser microirradiation experiment. (**B**) Representative images of endogenous DYRK1A with and without laser microirradiation. Cells are fixed 20 min after microirradiation and are then stained by primary and secondary antibody. Positions of damaged DNA are visualized by γH2AX staining. Arrows denote the microirradiation sites. Dotted lines indicate nuclei outlines. The percentage of DYRK1A stripe-positive cells over γH2AX stripe-positive cells are shown. (**C**) Full western blot of DYRK1A for U2OS control and DYRK1A knockout (KO)cells. * denotes non-specific band. (**D**) Schematic illustration of DYRK1A-full length (FL) and domain deletion mutants. Expressions of GFP-tagged DYRK1A derivatives are validated via Western blotting analysis. (**E**) Representative images of GFP-DYRK1A derivatives in U2OS cells before and after laser microirradiation. Arrows denote the laser microirradiation sites. Orange lines indicate the area chosen for reslice analysis of timelapse images. (**F**) Quantification of GFP-DYRK1A kinetics of (**E**). Error bars represent mean ± SEM from indicated number of nuclei of each sample. (**G**) Schematic illustration of RNF169, DYRK1A, and the binding-defective mutants. Co-immunoprecipitation (co-IP) blots indicate that DYRK1A-Δ91–113 and DYRK1A-Δ88–104 do not bind to RNF169. (**H**) Representative images of GFP-DYRK1A derivatives in microirradiated U2OS cells. Arrows denote the laser microirradiation sites. Orange lines indicate the area chosen for reslice analysis of timelapse images. (**I**) Quantification of GFP-DYRK1A kinetics of (H). Error bars represent mean ± SEM from indicated number of nuclei of each sample. (**J**) Representative images of GFP-DYRK1A-FL in U2OS cells before and after laser microirradiation upon indicated treatments. DMSO, ATM inhibitor (ATMi, 10μM KU55933 for 1 h), PARP inhibitor (PARPi, 10 μM Olaparib for 1 h) and ATMi + PARPi combined are applied before laser microirradiation. Arrows denote the laser microirradiation sites. Orange lines indicate the area chosen for reslice analysis of timelapse images. (**K**) Quantification of GFP-DYRK1A-FL kinetics of (J). Error bars represent mean ± SEM from indicated number of nuclei of each sample.

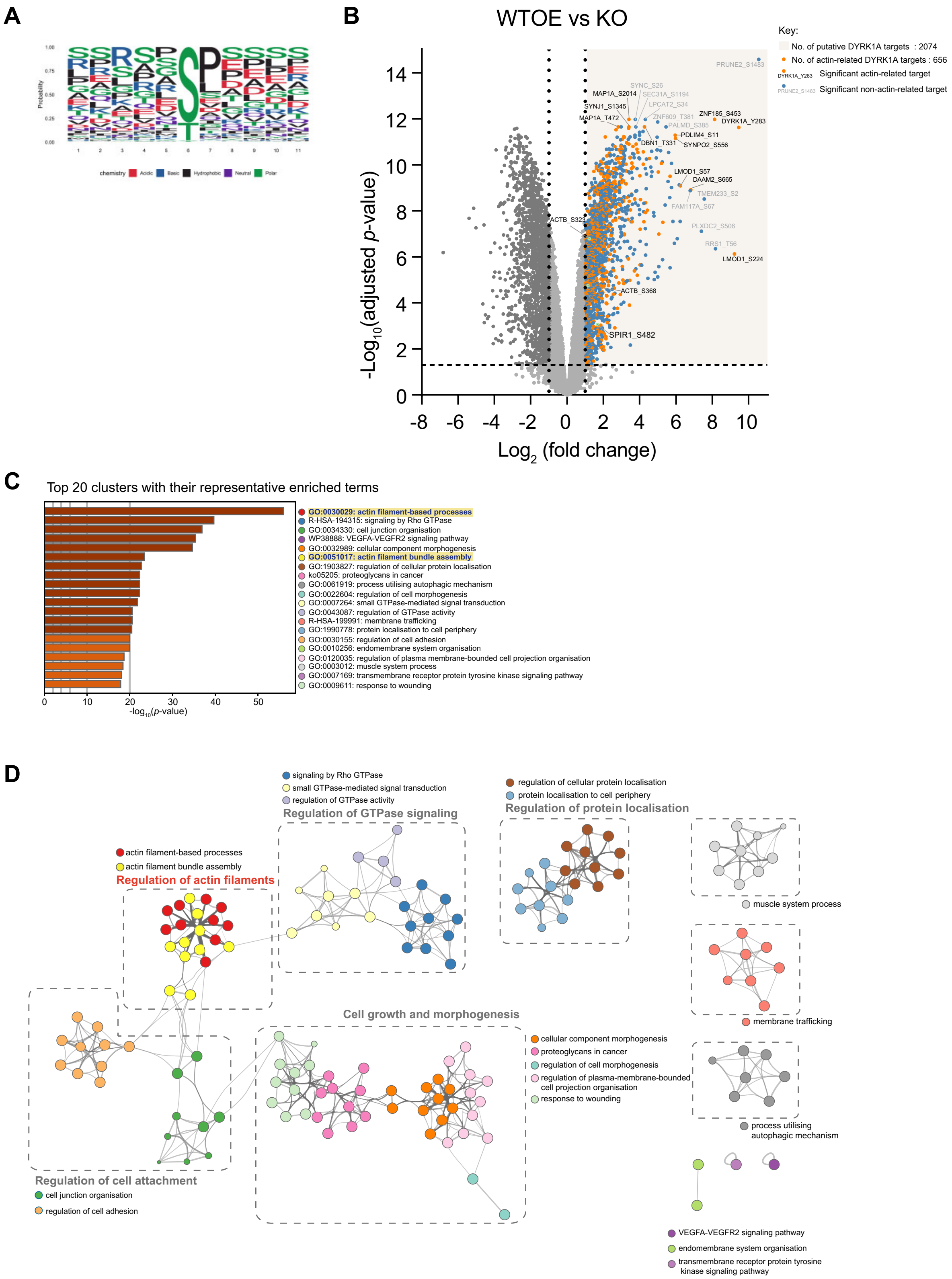

**Figure 2.** Phosphoproteome profiling links DYRK1A to actin organization control. (**A**) DYRK1A-targeting motifs determined from the shortlisted phospho-peptides identified in this study. (**B**) Volcano plots comparing DYRK1A-WT-OE phosphoproteome profiles to DYRK1A-KO counterpart. Each spot represents one phospho-peptide. Phospho-peptides which are with $\log_2$ fold change ≥1 and adjusted *P*-value ≤0.05 are defined as putative DYRK1A targets. Enriched phospho-peptides from known actin regulators are denoted in orange spots. Apart from Spir1_S482, ACTB_S323 and ACTB_S368, phosphopeptides with top 10 $-\log_{10}$ (adjusted *P*-values) and top 10 $\log_2$ (fold change) values are also labeled from the plot. (**C**) The top 20 enriched ontology clusters of the putative DYRK1A targets identified in this phospho-proteomic study. Pathway and process enrichment analysis are performed using the Metascape web-based portal (42). The enriched ontology terms are grouped into clusters based on their similarities. The clusters are ranked by $-\log_{10}$ (*P*-value). In each cluster, the ontology term with the smallest *P*-value is selected as the representative of the corresponding cluster. (**D**) The network plot of the top 20 enriched ontology clusters generated using the Metascape web-based portal (42). Each node represents an enriched ontology term. Terms with the same colour belong to the same cluster.

and were able to consistently detect enrichment of both probes at laser microirradiated sites, albeit with different kinetics (Figure 3A, B, Supplementary Figure S5C, D) (24,48). We took advantage of Utr230-EN due to its robustness in accumulating at DSBs (Nuclear expression pattern 2; see Figure 3A, B, Supplementary Figure S5C, D) in a manner that depended on PARP activity (Supplementary Figure S5E, F). Consistent with a role of DYRK1A in F-actin assembly at DSBs, loss of DYRK1A led to attenuated Utr230-EN accrual at laser-induced DSBs (Figure 3C–E). In line with a role of its kinase activity, we found that wildtype but not its kinase-inactive mutant complemented DYRK1A loss in supporting Utr230-EN enrichment at laser-induced DNA damage tracks (Figure 3C–E). Similarly, chemical inhibition of DYRK1A also attenuated F-actin assembly at DSBs (Figure 3F, G).

The actin-related protein 2/3 complex (Arp2/3) has previously been implicated in F-actin assembly at DSBs. Intriguingly, we found that chemical inhibition of Arp2/3 using CK666 compromised F-actin assembly at DSBs. Given that Utr230-EN enrichment at laser microirradiated sites was further exacerbated when CK666 was combined with DYRK1A deficiency (Figure 3H–J), we postulate that DYRK1A and Arp2/3 may cooperate to support full-blown F-actin assembly during DSB repair.

F-actin assembly on the damaged chromatin has been documented to drive DSB movements. To this end, we tested the effect of DYRK1A on DSB mobility by tracking DSB foci movements (49). Accordingly, we generated U2OS-DIvA cell line derivatives (Figure 4A) with stable expression of mCherry-tagged TP53-binding protein 1 (53BP1) or Partner and localizer of BRCA2 (PALB2), surrogate markers for NHEJ and HR repair, respectively (50). Because 53BP1 may serve roles beyond NHEJ, we focused our analyses on PALB2. Following a previously established approach (11), we induced DSBs and tracked the movement of mCherry foci, which denote the positions of damaged DNA (Figure 4B). We also included CK666-treated cells as positive control, as CK666 specifically inhibits actin-related protein 2/3 complex (Arp2/3) and in turn leads to suppressed DSB mobility (9,11). Accordingly, we compared the track length and found that DYRK1A loss impaired the mobility of PALB2- and 53BP1-marked DSBs (Figure 4C–E, Supplementary Figure S6, Movie S1). Moreover, clustering of PALB2-labeled DNA damage foci was also dependent on DYRK1A and Arp2/3 (Figure 4F–H, Movie S2). We concluded that DYRK1A promotes DSB mobility, and that this may be effected via local F-actin assembly at DSBs.

## Spir1 promotes F-actin formation at DSBs

Considering that DYRK1A supports DSB mobility and local F-actin formation, we reviewed the putative DYRK1A target list from our phospho-proteomic analysis, and identified the actin regulator Spir1 as a candidate DYRK1A effector (Supplementary Figure S7A). We confirmed that DYRK1A does indeed promote Spir1 phosphorylation as detected using anti pS/T-P antibodies (Supplementary Figure S7B). Given that both Spir proteins have been implicated in DSB repair (23) and the emerging interplay between FYVE domains and phosphatidylinositols on DSB-flanking chromatin (51), we first compared Spir1 and Spir2, and were intrigued by the presence of a putative NLS on the C-terminal FYVE domain of Spir1 (Supplementary Figure S7C). In support of a possible role of Spir1 in DSB responses, GFP-Spir1 FYVE predominantly resided in the nucleus, and was able to concentrate productively at laser-induced DNA damage tracks (Supplementary Figure S7D-E). We next analysed responsiveness of full-length Spir1 (GFP-Spir1) to laser microirradiation. GFP-tagged Spir1 proteins distributed across the entire cell, and we were only able to detect marginal accumulation of the protein at DSBs (Figure 5A-B, Supplementary Figure S8A-B) Notably, while GFP-Spir1 mobilized to laser-induced DSBs in a PARP-dependent manner, DYRK1 inhibition appears to result in more pronounced accumulation of Spir1 on the damaged chromatin (Supplementary Figure S8A, B). To corroborate this observation, we monitored GFP-Spir1 accumulation at laser-induced DSBs in DYRK1A knockout (KO) cells (Figure 5A–C). Consistently, we found more robust accumulation of GFP-Spir1 at DSBs in DYRK1A-depleted cells compared to its isogenic U2OS control cells (Figure 5A–C), suggesting that DYRK1A may promote Spir1 turnover from the damaged chromatin. To exclude off-target effect and to examine the requirement of DYRK1A kinase activity, we reconstituted DYRK1A KO cells with wildtype DYRK1A or its kinase inactive K188R mutant. Similar to DYRK1A-inhibited cells, GFP-Spir1 hyper-accumulated in cells expressing the K188R mutant allele (Figure 5A–C), suggesting that DYRK1A may indeed facilitate Spir1 dissociation from DSBs in a kinase-dependent manner.

## DYRK1A promotes Spir1 turnover at DSBs via phosphorylation at Spir1-S482

We next investigated the effect(s) of DYRK1A-dependent phosphorylation on Spir1 occupancy at DSBs. To this end, we generated the phospho-mimetic (S482D) and the phospho-dead (S482A) Spir1 mutants (Figure 5D). Consistent with a possible role of DYRK1A-dependent phosphorylation in negatively regulating Spir1 retention at DSBs, DSB recruitment of Spir1 S482D was attenuated when compared to either wildtype Spir1 or its phospho-dead S482A mutant (Figure 5E, F).

To further explore how Spir1 targets DSBs, we generated a panel of Spir1 deletion mutants (Supplementary Figure S9A), namely a KIND domain deletion mutant (ΔKIND) and a WH2 domain deletion mutant (ΔWH2). The Spir1 KIND and WH2 domains have been reported to mediate its interaction with FMN2 and actin, respectively (20,21,52). Intriguingly, the KIND domain deletion mutant (ΔKIND) was excluded from the nucleus, and was not noticeably detected at laser-induced DNA damage tracks (Supplementary Figure S9B, C). By contrast, we reproducibly observed more robust accumulation of ΔWH2 on the damaged chromatin, suggesting that the ability of Spir1 to target DSBs does not require its interaction with actin moieties, and that its inability to nucleate F-actin may lead to its prolonged association on the damaged chromatin. To test this idea, we depleted the actin nuclear import factor IPO9, and examined the recruitment kinetics of GFP-Spir1 at laser-induced DSBs. Consistently, we found that GFP-Spir1 accumulation was more pronounced in IPO9-inactivated cells (Supplementary Figure S9D, E). Similarly, chemical inhibition of Arp2/3 also led to more robust accumulation of Spir1 at DSBs (Supplementary Figure S9F, G). Interestingly, our observation that CK666 treatment did not affect S482D recruitment kinetics suggests that DYRK1A-dependent Spir1 phosphorylation is sufficient to promote its chromatin dissociation (Supplementary Figure S10A, B). Although the specificities of available anti-Spir1 antibodies

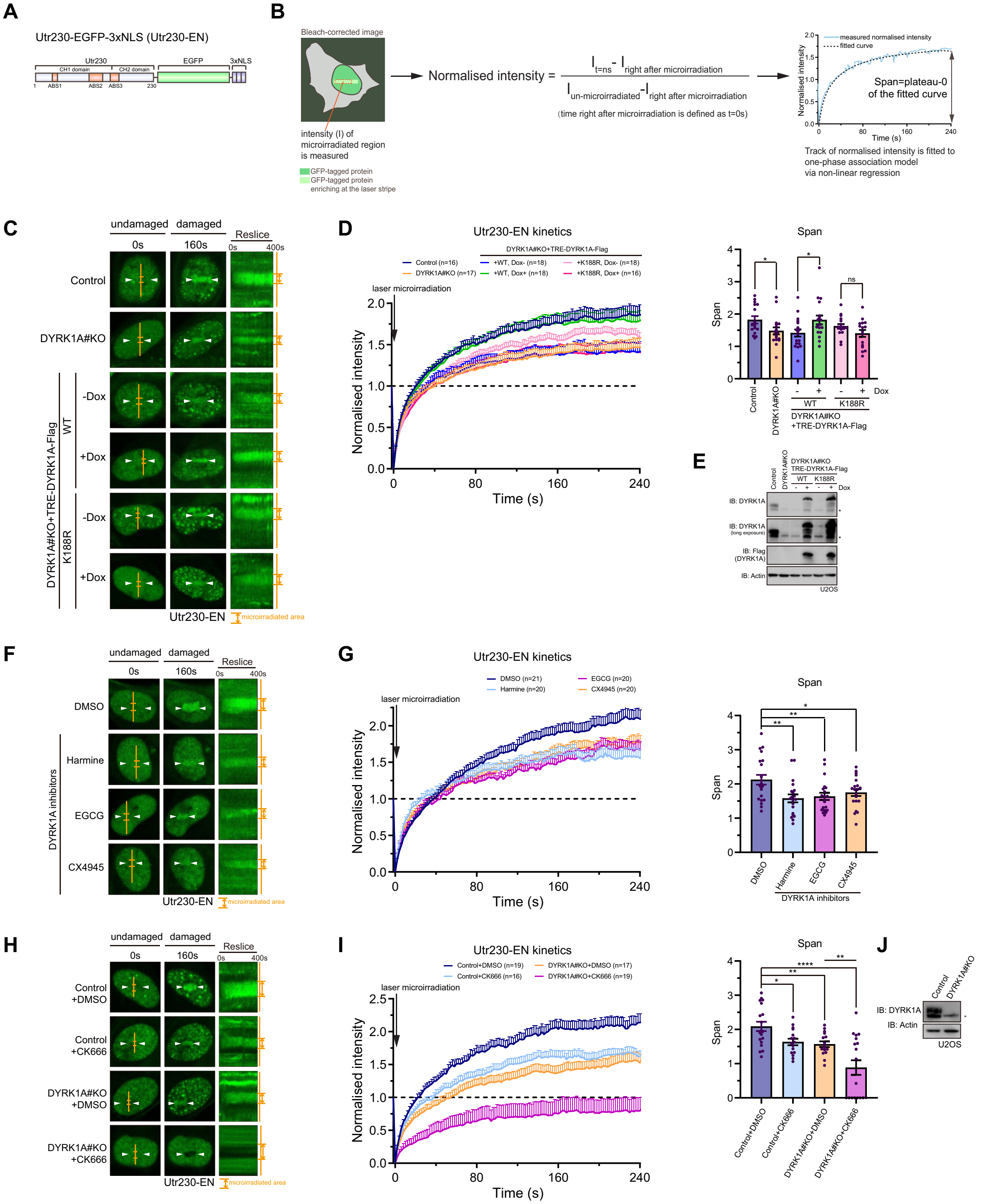

**Figure 3.** The DYRK1A kinase promotes actin assembly at DSBs. (**A**) Schematic illustration of Utr230-EGFP-3xNLS (Utr230-EN) as a nuclear F-actin marker. (**B**) Intensity quantification of timelapsed microirradiation data. Each normalised intensity track is fitted to one-phase association model. Span denotes plateau of the fitted curves. (**C**) Representative images of Utr230-EN in indicated U2OS derivatives before and after laser microirradiation. Ectopic DYRK1A expression is induced with 2 μg/ml doxycycline (Dox) for 24 h prior to microirradiation. Loss of DYRK1A lead to attenuated Utr230-EN accrual at laser-induced DSBs. Arrows denote the laser microirradiation sites. Orange lines indicate the area chosen for reslice analysis of timelapse images. (**D**) Quantification of Utr230-EN kinetics and summarised span of (C). Error bars represent mean ± SEM from indicated numbers of nuclei of each sample. $*P \leq 0.05$; ns, non-significant. (**E**) Western blotting analysis of U2OS derivatives used in (C) and (D). *, non-specific band. (**F**) Representative images of Utr230-EN in DYRK1A-inhibited U2OS cells. DYRK1A inhibitors, including harmine (10 μM for 1 h), EGCG (2.5 μM for 3 h) and CX4945 (10 μM for 1 h), attenuate F-actin assembly at DSBs. Arrows denote the laser microirradiation sites. Orange lines indicate the area chosen for reslice analysis of timelapse images. (**G**) Quantification of Utr230-EN kinetics and summarized span of (F). Error bars represent mean ± SEM from indicated numbers of nuclei of each sample. $*P \leq 0.05$; $**P \leq 0.01$. (**H**) Representative images of Utr230-EN in indicated U2OS derivatives. Arp2/3 complex inhibitor CK666 (100 μM for 1 h prior to laser microirradiation) compromises F-actin assembly at DSBs. Arrows denote the laser microirradiation sites. Orange lines indicate the area chosen for reslice analysis of timelapse images. (**I**) Quantification of Utr230-EN kinetics and summarised span of (H). Error bars represent mean ± SEM from indicated numbers of nuclei of each sample. $*P \leq 0.05$; $**P \leq 0.01$, $***P \leq 0.001$. (**J**) Western blotting analysis of (H) and (I). *, non-specific band.

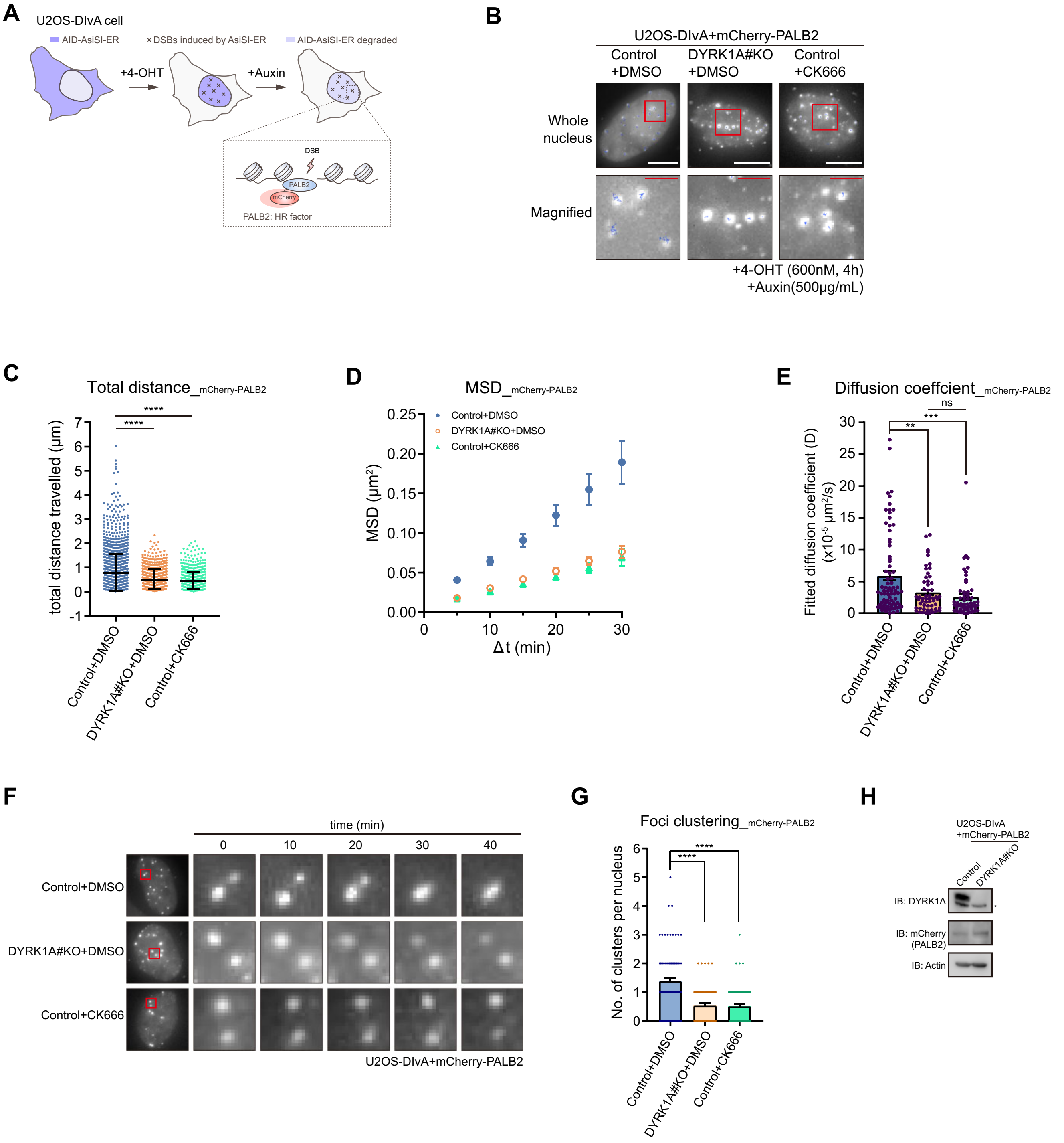

**Figure 4.** DYRK1A promotes DSB foci dynamics. (**A**) Schematic illustration of DSB foci tracking experiments using U2OS-DIvA with stable expression of mCherry-PALB2. DSBs are induced with 600nM 4-OHT for 4 h. The AsisI-ER degradation is achieved using 500 μg Auxin incubation for 1 h. (**B**) mCherry-PALB2 DSB foci in U2OS-DIvA derivatives. DYRK1A loss and Arp2/3 inhibition impair the DSB mobility. CK666 (100 μM for 1 h) or DMSO is applied prior to live cell imaging (5-min intervals for 50 min). Traces of mCherry-PALB2 in the nucleus are shown in the magnified panel. White and red scale bars represent 10 μm and 2 μm, respectively. (**C**) Quantification of total distance travelled, and (**D**) mean square displacement (MSD), of PALB2-marked foci. Error bars represent mean ± SD (C) and; mean ± SEM (D), respectively. $^{****}P \leq 0.0001$. (**E**) Diffusion coefficients for (D). Error bars represent mean ± SEM. $^{**}P \leq 0.01$; $^{***}P \leq 0.001$; ns, non-significant. (**F**) Representative timelapse images of mCherry-PALB2 foci clustering in indicated U2OS-DIvA derivatives. DYRK1A loss and Arp2/3 inhibition suppress the clustering of DSB foci. Regions in red boxes are magnified for presentation of foci dynamics. A clustering event is defined as colocalization of at least two foci for at least three consecutive frames. (**G**) Quantification of mCherry-PALB2 clustering events for (A). Error bars represent mean ± SEM of the stated numbers of nuclei (see Supplementary Figure S6A) collected from three independent experiments. $^{****}P \leq 0.0001$. (**H**) Western blotting analysis of (B)–(G). *, non-specific band.

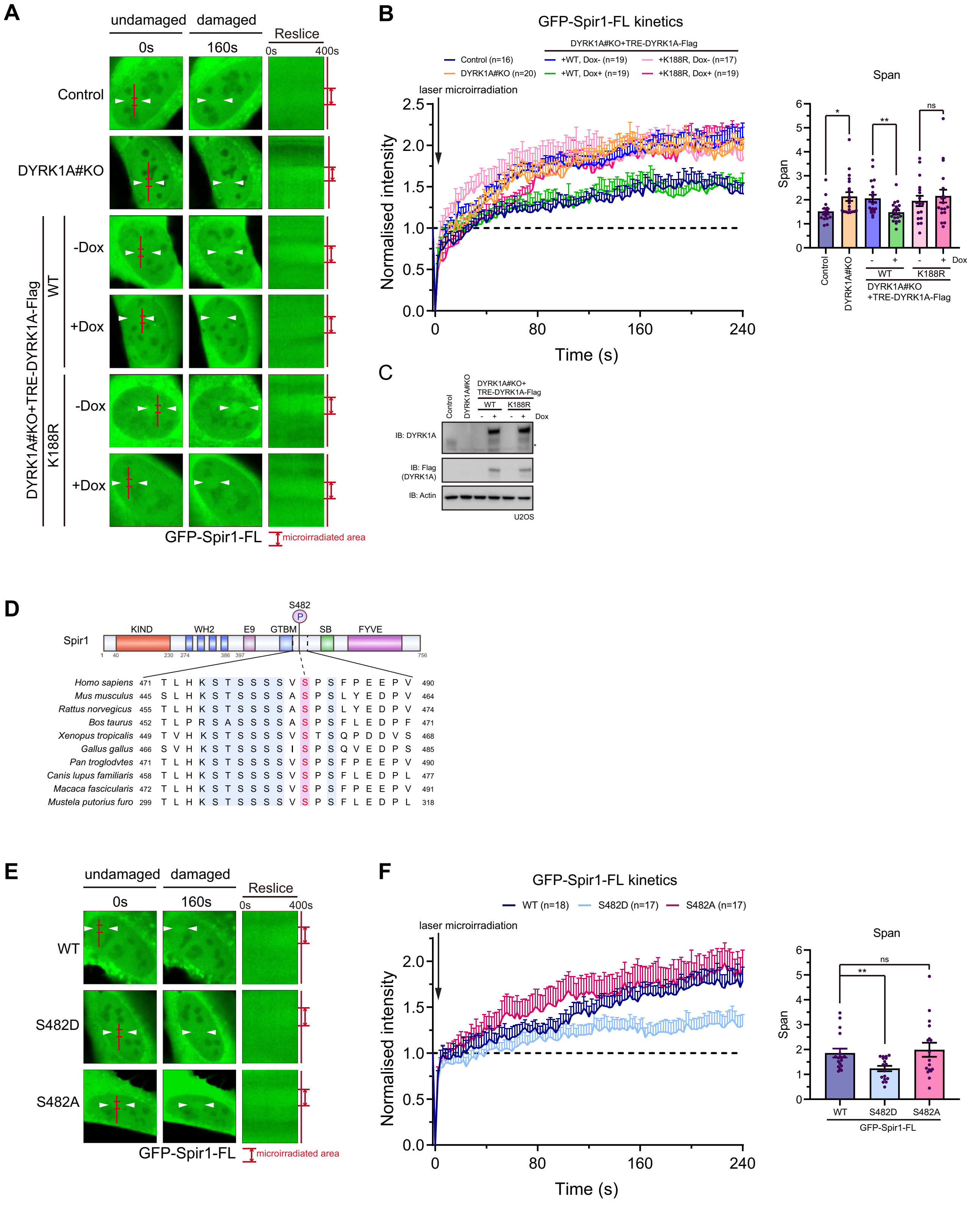

**Figure 5.** DYRK1A regulates Spir1 accumulation at DSBs. (**A**) Representative images of GFP-Spir1-FL (full-length) in indicated U2OS derivatives. Robust accumulation of GFP-Spir1-FL at DSBs in DYRK1A-inactivated cells. Ectopic DYRK1A expression is induced with 2 μg/ml doxycycline (Dox) for 24 h prior to microirradiation. Arrows denote the laser microirradiation sites. Red lines indicate the area chosen for reslice analysis of timelapse images. (**B**) Quantification of GFP-Spir1-FL kinetics and summarized span of (A). Error bars represent mean ± SEM from indicated numbers of nuclei of each sample. $*P \leq 0.05$; $**P \leq 0.01$; ns, non-significant. (**C**) Western blotting analysis of (A) and (B). *, non-specific band. (**D**) Schematic illustration of human Spir1 domains with S482 position (upper panel), and multiple sequence alignment of Spir1 orthologues at the sequence flanking human Spir1-S482 (lower panel). (**E**) Representative images of GFP-Spir1-FL derivatives in U2OS cells. DSB recruitment of Spir1 S482D is significantly attenuated. Arrows denote the laser microirradiation sites. Red lines indicate the area chosen for reslice analysis of timelapse images. (**F**) Quantification of indicated GFP-Spir1-FL derivatives kinetics and summarized span of (E). Error bars represent mean ± SEM from indicated numbers of nuclei of each sample. $**P \leq 0.01$; ns, non-significant.

precluded us from examining the responsiveness of endogenous Spir1 to DSBs by indirect immunofluorescence studies (Supplementary Figure S11A–C), these observations support the idea that Spir1 participates in DSB responses by targeting the damaged chromatin, and that DYRK1A-dependent phosphorylation of Spir1 may regulate its occupancy and dynamics at DSBs.

### DYRK1A cooperates with Spir1 to promote local F-actin formation and DSB repair

To test if DYRK1A and Spir1 may be epistatic in DSB-associated F-actin assembly, we generated Spir1 KO cells, as well as Spir1 and DYRK1A double KO cells. In resemblance to DYRK1A-ablated cells, Spir1 deficiency led to attenuated F-actin formation at DSBs (Figure 6A–C), and resulted in persistent DNA damage foci (Supplementary Figure S12A–C). When compared to the cells with either DYRK1A ablation or Spir1 depletion alone, the DYRK1A and Spir1 double knockout cells did not show further aggravation in these phenotypes (Figure 6A–C, Supplementary Figure S12A–C). Moreover, similar to Spir1, IPO9 inactivation attenuated F-actin assembly and DNA damage foci clearance to the same extent as combined loss of IPO9 and DYRK1A (Figure 6D–F, Supplementary Figure S12D–F), supporting the nuclear-specific role of DYRK1A in promoting DSB-associated actin polymerization. Together, these findings further corroborated that DYRK1A and Spir1 participate in the same pathway to regulate nuclear F-actin assembly and DSB repair.

To further examine the importance of DYRK1A-dependent Spir1 phosphorylation in DSB responses, we first reconstituted Spir1 KO cells with the wildtype Spir1 allele, and optimized conditions that would allow ectopically expressed Spir1 to support F-actin assembly on the damaged chromatin in otherwise Spir1-deficient cells (Supplementary Figure S13A–C). Intriguingly, we found that neither the phospho-mimicking nor the phospho-dead Spir1 mutant complemented loss of Spir1 in either DSB-associated F-actin assembly (Figure 6G-I) or DNA damage foci clearance in either wildtype background (Supplementary Figure S14A–C) or DYRK1A-deficient background (Supplementary Figure S15A-C), pointing to a role of DYRK1A in regulating the Spir1-dependent actin nucleating via a phosphorylation and dephosphorylation cycle on the damaged chromatin.

## Discussion

Increased mobility of DSB chromatin domains facilitates DNA repair, but the molecular details that drive the nuclear response remain to be defined. Here we have uncovered DYRK1A as a nuclear activity that fuels DSB mobilization and repair. The requirement of DYRK1A kinase activity in promoting genome stability (Supplementary Figure S2) also led us to identify the actin nucleating factor Spir1 as a *bona fide* DYRK1A target (Figure 2B; Supplementary Figure S7A), where we show that DYRK1A promotes Spir1 phosphorylation at S482 to prevent its otherwise sustained accumulation on the damaged chromatin. Indeed, in reminiscence to ‘trapping’ of catalytically-inactive DNA damage signaling factors at DSBs (53,54), genetic or chemical inactivation of IPO9, Spir1 or Arp2/3 led to substantial increase in fraction of cells with visible DYRK1A accumulation at laser-induced DNA damage tracks (Supplementary Figure S16A–C), further supporting the notion that DYRK1A encodes a nuclear activity that fuels F-actin assembly at DSBs. We propose that such regulation ensures dynamic Spir1 activity at DSBs and underlies productive F-actin assembly on the damaged chromatin (Figure 7).

While all three classes of major actin nucleator proteins, namely Arp2/3, formins and Spire, have been implicated in DNA repair processes (9,11,13,19,23), it has remained unclear how Spire proteins promote F-actin assembly on the damaged chromatin. Here we found that Spir1 targets DSBs via its FYVE domain (Supplementary Figure S7C–E), and that DYRK1A-dependent Spir1 phosphorylation is key to the regulation of Spir1 dynamics at DSBs. The proposal is based on the fact that genetic inactivation of DYRK1A or chemical inhibition of its kinase activity led to hyper-accumulation of Spir1 at laser-induced DSBs (Figure 5A–C, Supplementary Figure S8). In agreement, while S482D attenuated Spir1 accumulation at laser-induced DNA damage tracks, the phospho-dead S482A mutant was more readily mobilized onto the damaged chromatin (Figure 5E, F). Although how Spir1 phosphorylation/dephosphorylation cycle underlies F-actin assembly remains to be elucidated, we posit that S482 phosphorylation may allosterically regulate Spir1 occupancy on the damaged chromatin. We envisage that Spir1 serves its actin nucleating role by concentrating actin monomers to DNA damage sites via its actin binding WH2 repeats. Such working model would predict that Spir1 undergoes dynamic association and dissociation to permit productive actin polymerization. Moreover, that both Spir1 S482A and S482D exhibited perturbed recruitment kinetics to laser-induced DNA damage tracks, and that neither supported DSB-induced F-actin formation (Figure 6G–I) or DNA damage foci clearance (Supplementary Figure S14A–C) highlight the importance of Spir1 dynamics at DSBs in effective local nuclear F-actin assembly, and unequivocally underlines its function in DSBs responses (Figure 7).

Considering the contrasting difference between full-length Spir1 and its FYVE in docking at DSBs, one would envisage that Spir1 actin nucleating activity may be one of the determinants that underlie its kinetics at DSBs, a preposition that is supported by our observations wherein inactivating of either Spir1 WH2 repeats and actin nuclear importer IPO9 similarly led to Spir1 ‘hyperaccumulation’ on the damaged chromatin (Supplementary Figure S9A–D). Given that FYVE domains are endowed with affinities for phosphatidylinositol phosphates (PIPs), and that PIPs have implicated roles in DNA damage signal transduction (24,55), it would be of interest to study how Spir1 FYVE interacts with DSB-associated PIPs, and to identify the specific PIP(s) that Spir1 FYVE interacts with to appreciate the emerging interplay of DNA damage-induced actin polymerization and PIPs on the damaged chromatin.

In summary, we have identified the DYRK1A kinase as a nuclear regulator of actin nucleator Spir1. Our findings suggest that DYRK1A targets Spir1 on the damaged chromatin to drive its recycling to facilitate actin polymerization that effects DNA repair.

## Data availability

The phospho-proteomic data generated in this study have been uploaded to ProteomeXchange, project accession number: PXD031714.

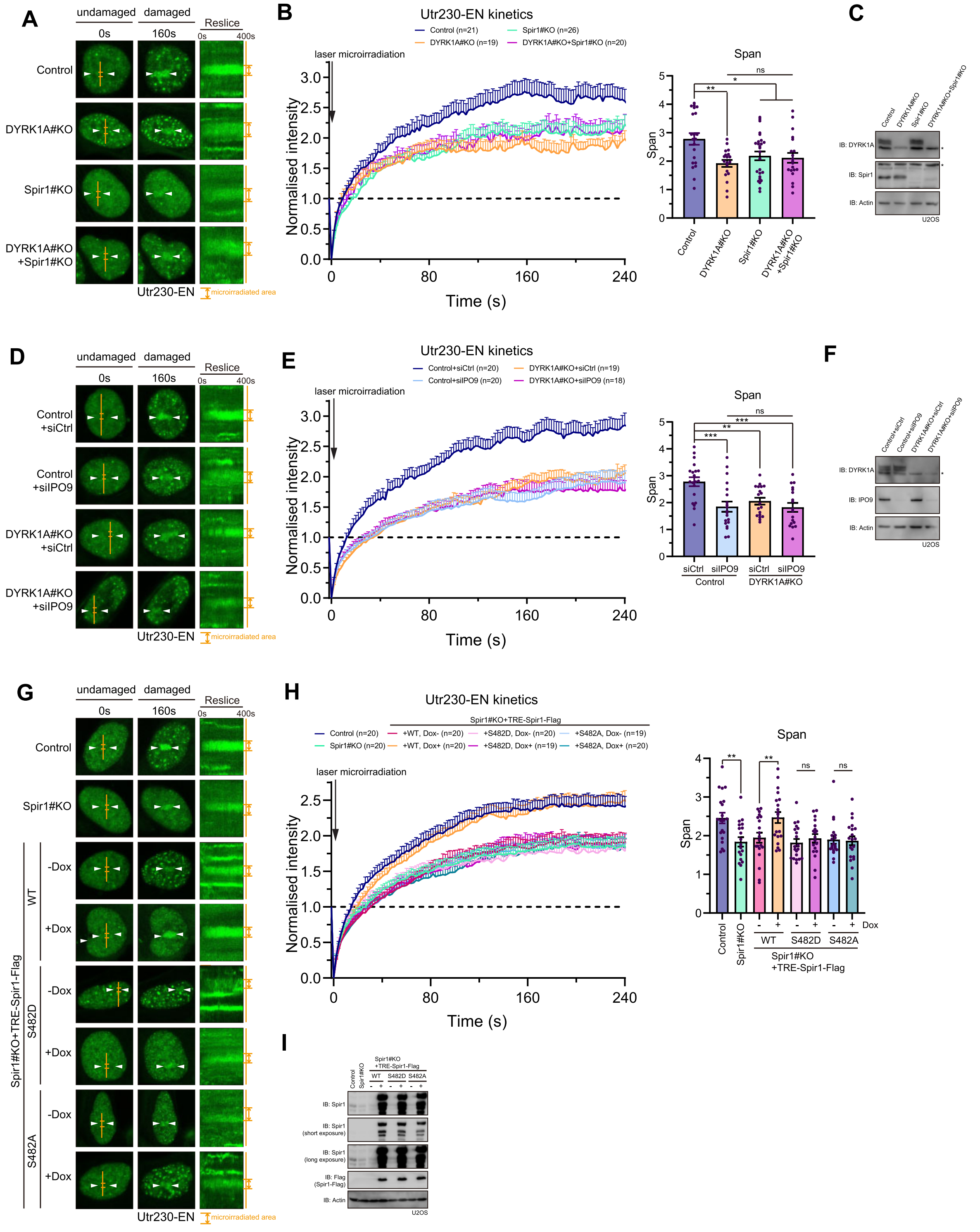

**Figure 6.** DYRK1A-dependent actin dynamics at DSBs requires Spir1. (**A**) Representative images of Utr230-EN in microirradiated U2OS with DYRK1A depleted, Spir1 ablated, and DYRK1A-Spir1 double knockout (KO), respectively. The deficiency of either DYRK1A or Spir1 leads to similar attenuation of F-actin formation at DSBs. Arrows denote the laser microirradiation sites. Orange lines indicate the area chosen for reslice analysis of timelapse images. (**B**) Quantification of Utr230-EN kinetics and summarized span of (A). Error bars represent mean ± SEM from indicated numbers of nuclei of each sample. *, $p \leq 0.05$; **, $p \leq 0.01$; ns, non-significant. (**C**) Western blotting analysis of (A) and (B). *, non-specific band. (**D**) Representative images of Utr230-EN in control and DYRK1A-KO cells with IPO9 inactivation. Knockdown of IPO9 attenuates F-actin assembly at DSBs. Arrows denote the laser microirradiation sites. Orange lines indicate the area chosen for reslice analysis of timelapse images. (**E**) Quantification of Utr230-EN kinetics and summarized span of (D). Error bars represent mean ± SEM from indicated numbers of nuclei of each sample. $^{**}P \leq 0.01$; $^{***}P \leq 0.001$; ns, non-significant. (**F**) Western blotting analysis of (D) and (E). *, non-specific band. (**G**) Representative images of Utr230-EN in indicated U2OS derivatives. Ectopic Spir1-Flag expression was induced with 2 μg doxycycline (Dox) for 24 h prior to laser microirradiation. Neither the phospho-mimicking nor the phospho-dead Spir1 mutant complements the loss of Spir1 in DSB-associated F-actin assembly. Arrows denote the laser microirradiation sites. Orange lines indicate the area chosen for reslice analysis of timelapse images. (**H**) Quantification of Utr230-EN kinetics and summarized span of (**G**). Error bars represent mean ± SEM from indicated numbers of nuclei of each sample. $^{*}P \leq 0.05$; ns, non-significant. (**I**) Western blotting analysis of (G) and (H).

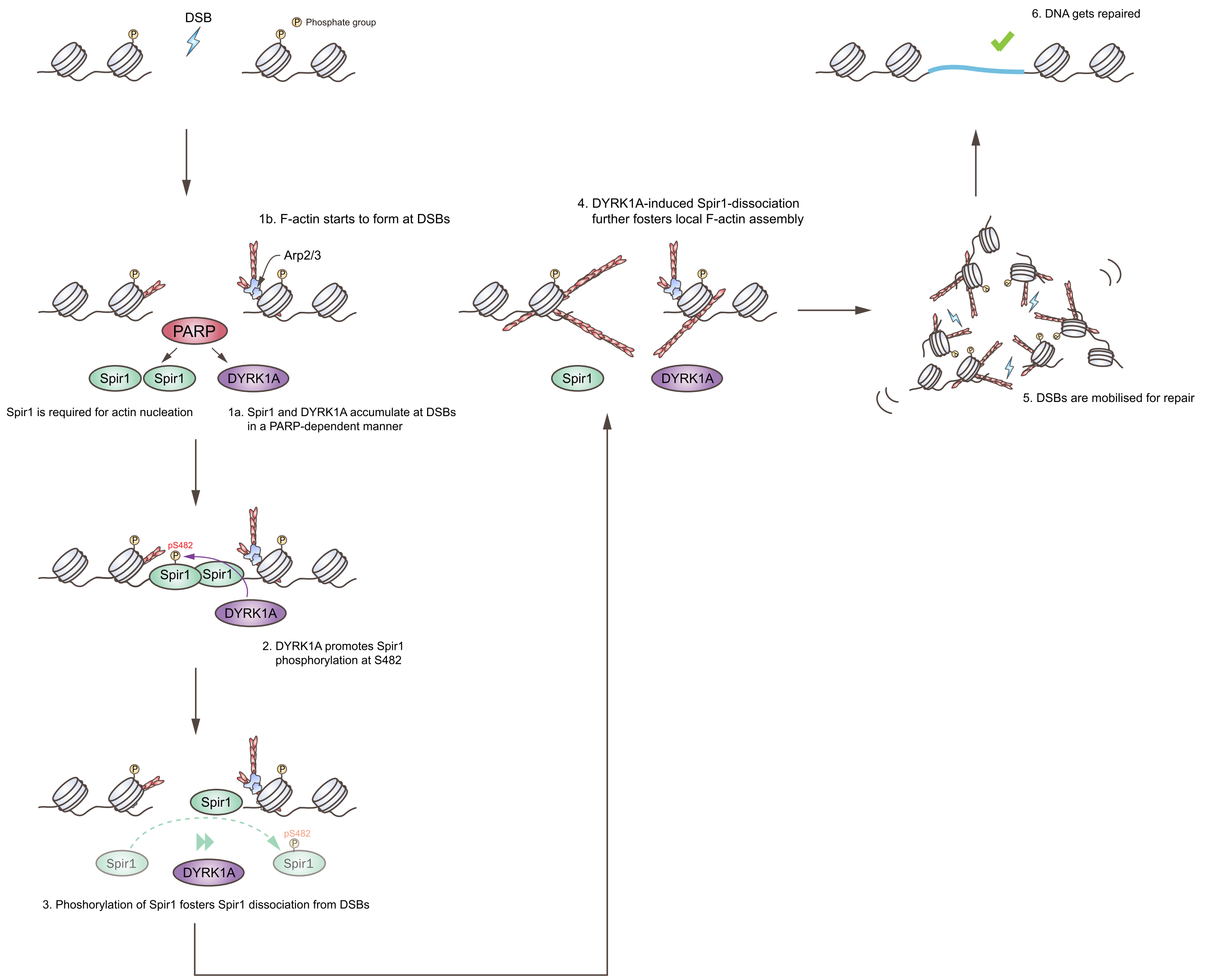

**Figure 7.** Working model**.** Schematic of working model. Upon enrichment at DNA double-strand break (DSB), DYRK1A mediates Spir1 phosphorylation at S482 and promotes its dissociation from DSBs. DYRK1A works together with Spir1 to foster local F-actin assembly for DSB movement and repair.

## Supplementary data

Supplementary Data are available at NAR Online.

## Acknowledgements

We thank Dr Gaëlle Legube for generous sharing of U2OS-DIvA cells, and Dr Susana de la Luna for critical reading and insightful comments on the manuscript. We also acknowledge the technical support from Centre for PanorOmic Sciences (The University of Hong Kong).

*Author contribution:* J.L., J.W.C.L. and M.S.Y.H. designed experiments. J.L., X.N. and K.L.W. carried out experiments and data analysis. M.H.M.L. and C.H.Y. provided expertise in data analyses. J.H., J.Y., Y.P.C, C.H.Y., J.W.C.L. provided resources and advice. M.S.Y.H. supervised this work. J.L. and M.S.Y.H. wrote the manuscript, with input from all authors.

## Funding

Research Grants Council Hong Kong [17100520, 17103522, T12-702/20/N, N_HKU722/19] to M. Huen; J. Leung is supported by National Institutes of Health/National Institute of General Medical Sciences (NIH/NIGMS) [R35GM137798]; National Institutes of Health/National Cancer Institute (NIH/NCI) [R01CA244261]; American Cancer Society [RSG-20-131-01-DMC, TLC-21-164-01-TLC]; K. West is supported by the American Cancer Society [PF-21-083-01-DMC]. Funding for open access charge: Research Grants Council, University Grants Committee.

## Conflict of interest statement

None declared.

## References

1. Ceccaldi,R., Rondinelli,B. and D'Andrea,A.D. (2014) Repair pathway choices and consequences at the double-strand break. *Trends Cell Biol.*, **26**, 52–64.
2. Maréchal,A. and Zou,L. (2013) DNA damage sensing by the ATM and ATR kinases. *Cold Spring Harb. Perspect. Biol.*, **5**, a012716.
3. Cho,N.W., Dilley,R.L., Lampson,M.A. and Greenberg,R.A. (2014) Interchromosomal homology searches drive directional ALT telomere movement and synapsis. *Cell*, **159**, 108–121.

4. Heun,P., Laroche,T., Shimada,K., Furrer,P. and Gasser,S.M. (2001) Chromosome dynamics in the yeast interphase nucleus. *Science*, **294**, 2181–2186.
5. Marshall,W.F., Straight,A., Marko,J.F., Swedlow,J., Dernburg,A., Belmont,A., Murray,A.W., Agard,D.A. and Sedat,J.W. (1997) Interphase chromosomes undergo constrained diffusional motion in living cells. *Curr. Biol.*, **7**, 930–939.
6. Dion,V., Kalck,V., Horigome,C., Towbin,B.D. and Gasser,S.M. (2012) Increased mobility of double-strand breaks requires Mec1, Rad9 and the homologous recombination machinery. *Nat. Cell Biol.*, **14**, 502–509.
7. Neumann,F.R., Dion,V., Gehlen,L.R., Tsai-Pflugfelder,M., Schmid,R., Taddei,A. and Gasser,S.M. (2012) Targeted INO80 enhances subnuclear chromatin movement and ectopic homologous recombination. *Genes Dev.*, **26**, 369–383.
8. Miné-Hattab,J. and Rothstein,R. (2012) Increased chromosome mobility facilitates homology search during recombination. *Nat. Cell Biol.*, **14**, 510–517.
9. Caridi,C.P., D'Agostino,C., Ryu,T., Zapotoczny,G., Delabaere,L., Li,X., Khodaverdian,V.Y., Amaral,N., Lin,E., Rau,A.R., *et al.* (2018) Nuclear F-actin and myosins drive relocalization of heterochromatic breaks. *Nature*, **559**, 54–60.
10. Cheblal,A., Challa,K., Seeber,A., Shimada,K., Yoshida,H., Ferreira,H.C., Amitai,A. and Gasser,S.M. (2020) DNA damage-induced nucleosome depletion enhances homology search independently of local break movement. *Mol. Cell*, **80**, 311–326.
11. Schrank,B.R., Aparicio,T., Li,Y., Chang,W., Chait,B.T., Gundersen,G.G., Gottesman,M.E. and Gautier,J. (2018) Nuclear ARP2/3 drives DNA break clustering for homology-directed repair. *Nature*, **559**, 61–66.
12. Horigome,C., Oma,Y., Konishi,T., Schmid,R., Marcomini,I., Hauer,M.H., Dion,V., Harata,M. and Gasser,S.M. (2014) SWR1 and INO80 chromatin remodelers contribute to DNA double-strand break perinuclear anchorage site choice. *Mol. Cell*, **55**, 626–639.
13. Aymard,F., Aguirrebengoa,M., Guillou,E., Javierre,B.M., Bugler,B., Arnould,C., Rocher,V., Iacovoni,J.S., Biernacka,A., Skrzypczak,M., *et al.* (2017) Genome-wide mapping of long-range contacts unveils clustering of DNA double-strand breaks at damaged active genes. *Nat. Struct. Mol. Biol.*, **24**, 353–361.
14. Chiolo,I., Minoda,A., Colmenares,S.U., Polyzos,A., Costes,S.V. and Karpen,G.H. (2011) Double-strand breaks in heterochromatin move outside of a dynamic HP1a domain to complete recombinational repair. *Cell*, **144**, 732–744.
15. Strickfaden,H., McDonald,D., Kruhlak,M.J., Haince,J.F., Th'ng,J.P.H., Rouleau,M., Ishibashi,T., Corry,G.N., Ausio,J., Underhill,D.A., *et al.* (2016) Poly(ADP-ribosyl)ation-dependent transient chromatin decondensation and histone displacement following laser microirradiation. *J. Biol. Chem.*, **291**, 1789–1802.
16. Dimitrova,N., Chen,Y.-C.M., Spector,D.L. and de Lange,T. (2008) 53BP1 promotes non-homologous end joining of telomeres by increasing chromatin mobility. *Nature*, **456**, 524–528.
17. Lottersberger,F., Karssemeijer,R.A., Dimitrova,N. and de Lange,T. (2015) 53BP1 and the LINC complex promote microtubule-dependent DSB mobility and DNA repair. *Cell*, **163**, 880–893.
18. Oshidari,R., Strecker,J., Chung,D.K.C., Abraham,K.J., Chan,J.N.Y., Damaren,C.J. and Mekhail,K. (2018) Nuclear microtubule filaments mediate non-linear directional motion of chromatin and promote DNA repair. *Nat. Commun.*, **9**, 2567.
19. Goley,E.D. and Welch,M.D. (2006) The ARP2/3 complex: an actin nucleator comes of age. *Nat. Rev. Mol. Cell Biol.*, **7**, 713–726.
20. Quinlan,M.E., Heuser,J.E., Kerkhoff,E. and Mullins,R. (2005) Drosophila Spire is an actin nucleation factor. *Nature*, **433**, 382–388.
21. Vizcarra,C.L., Kreutz,B., Rodal,A.A., Toms,A.V., Lu,J., Zheng,W., Quinlan,M.E. and Eck,M.J. (2011) Structure and function of the interacting domains of Spire and Fmn-family formins. *Proc. Nat. Acad. Sci. U.S.A.*, **108**, 11884–11889.
22. Quinlan,M.E., Hilgert,S., Bedrossian,A., Mullins,R.D. and Kerkhoff,E. (2007) Regulatory interactions between two actin nucleators, Spire and Cappuccino. *J. Cell Biol.*, **179**, 117–128.
23. Belin,B.J., Lee,T. and Mullins,R.D. (2015) DNA damage induces nuclear actin filament assembly by Formin -2 and Spire-$\frac{1}{2}$ that promotes efficient DNA repair. *eLife*, **4**, e07735.
24. Wang,Y.-H., Hariharan,A., Bastianello,G., Toyama,Y., Shivashankar,G.V., Foiani,M. and Sheetz,M.P. (2017) DNA damage causes rapid accumulation of phosphoinositides for ATR signaling. *Nat. Commun.*, **8**, 2118.
25. Park,J., Song,W.-J. and Chung,K.C. (2009) Function and regulation of Dyrk1A: towards understanding Down syndrome. *Cell. Mol. Life Sci.*, **66**, 3235–3240.
26. Chen,J.-Y., Lin,J.-R., Tsai,F. and Meyer,T. (2013) Dosage of Dyrk1a shifts cells within a p21-cyclin D1 signaling map to control the decision to enter the cell cycle. *Mol. Cell*, **52**, 87–100.
27. Liu,Q., Tang,Y., Chen,L., Liu,N., Lang,F., Liu,H., Wang,P. and Sun,X. (2016) E3 ligase SCF$^{\beta\ \mathrm{TrCP}}$-induced DYRK1A protein degradation is essential for cell cycle progression in HEK293 cells. *J. Biol. Chem.*, **291**, 26399–26409.
28. Laguna,A., Aranda,S., Barallobre,M., Barhoum,R., Fernández,E., Fotaki,V., Delabar,J., de la Luna,S., de la Villa,P. and Arbonés,M. (2008) The protein kinase DYRK1A regulates caspase-9-mediated apoptosis during retina development. *Dev. Cell*, **15**, 841–853.
29. Di Vona,C., Bezdan,D., Islam,A.B., Salichs,E., López-Bigas,N., Ossowski,S. and de la Luna,S. (2015) Chromatin-wide profiling of DYRK1A reveals a role as a gene-specific RNA polymerase II CTD kinase. *Mol. Cell*, **57**, 506–520.
30. Roewenstrunk,J., Di Vona,C., Chen,J., Borras,E., Dong,C., Arató,K., Sabidó,E., Huen,M. and de la Luna,S. (2019) A comprehensive proteomics-based interaction screen that links DYRK1A to RNF169 and to the DNA damage response. *Sci. Rep.*, **9**, 6014.
31. Menon,V.R., Ananthapadmanabhan,V., Swanson,S., Saini,S., Sesay,F., Yakovlev,V., Florens,L., DeCaprio,J.A., Washburn,M.P., Dozmorov,M., *et al.* (2019) DYRK1A regulates the recruitment of 53BP1 to the sites of DNA damage in part through interaction with RNF169. *Cell Cycle*, **18**, 531–551.
32. Guard,S.E., Poss,Z.C., Ebmeier,C.C., Pagratis,M., Simpson,H., Taatjes,D.J. and Old,W.M. (2019) The nuclear interactome of DYRK1A reveals a functional role in DNA damage repair. *Sci. Rep.*, **9**, 6539.
33. Stoler-Barak,L., Harris,E., Peres,A., Hezroni,H., Kuka,M., Di Lucia,P., Grenov,A., Gurwicz,N., Kupervaser,M., Yip,B.H., *et al.* (2023) B cell class switch recombination is regulated by DYRK1A through MSH6 phosphorylation. *Nat. Commun.*, **14**, 1462.
34. Iacovoni,J.S., Caron,P., Lassadi,I., Nicolas,E., Massip,L., Trouche,D. and Legube,G. (2010) High-resolution profiling of gammaH2AX around DNA double strand breaks in the mammalian genome. *EMBO J.*, **29**, 1446–1457.
35. Aymard,F., Bugler,B., Schmidt,C.K., Guillou,E., Caron,P., Briois,S., Iacovoni,J.S., Daburon,V., Miller,K.M., Jackson,S.P., *et al.* (2014) Transcriptionally active chromatin recruits homologous recombination at DNA double-strand breaks. *Nat. Struct. Mol. Biol.*, **21**, 366–374.
36. Sanjana,N.E., Shalem,O. and Zhang,F. (2014) Improved vectors and genome-wide libraries for CRISPR screening. *Nat. Methods*, **11**, 783–784.
37. Shalem,O., Sanjana,N.E., Hartenian,E., Shi,X., Scott,D.A., Mikkelsen,T., Heckl,D., Ebert,B.L., Root,D.E., Doench,J.G. and Zhang,F. (2014) Genome-scale CRISPR-Cas9 knockout screening in human cells. *Science*, **343**, 83–87.
38. Schindelin,J., Arganda-Carreras,I., Frise,E., Kaynig,V., Longair,M., Pietzsch,T., Preibisch,S., Rueden,C., Saalfeld,S., Schmid,B., *et al.* (2012) Fiji: an open-source platform for biological-image analysis. *Nat. Methods*, **9**, 676–682.
39. Tarantino,N., Tinevez,J.-Y., Crowell,E.F., Boisson,B., Henriques,R., Mhlanga,M., Agou,F., Israël,A. and Laplantine,E. (2014) TNF and IL-1 exhibit distinct ubiquitin requirements for inducing

NEMO-IKK supramolecular structures. *J. Cell Biol.*, **204**, 231–245.

40. Dong,C., West,K.L., Tan,X.Y., Li,J., Ishibashi,T., Yu,C.H., Sy,S., Leung,J. and Huen,M. (2020) Screen identifies DYRK1B network as mediator of transcription repression on damaged chromatin. *Proc. Nat. Acad. Sci. U.S.A.*, **117**, 17019–17030.
41. Zybailov,B.L., Glazko,G.V., Rahmatallah,Y., Andreyev,D.S., McElroy,T., Karaduta,O., Byrum,S.D., Orr,L., Tackett,A.J., Mackintosh,S.G., *et al.* (2019) Metaproteomics reveals potential mechanisms by which dietary resistant starch supplementation attenuates chronic kidney disease progression in rats. *PLoS One*, **14**, e0199274.
42. Zhou,Y., Zhou,B., Pache,L., Chang,M., Khodabakhshi,A.H., Tanaseichuk,O., Benner,C. and Chanda,S.K. (2019) Metascape provides a biologist-oriented resource for the analysis of systems-level datasets. *Nat. Commun.*, **10**, 1523.
43. Lan,B., Zeng,S., Zhang,S., Ren,X., Xing,Y., Kutschick,I., Pfeffer,S., Frey,B., Britzen-Laurent,N., Grützmann,R., *et al.* (2022) CRISPR-Cas9 screen identifies DYRK1A as a target for radiotherapy sensitization in pancreatic cancer. *Cancers (Basel)*, **14**, 326.
44. Himpel,S., Tegge,W., Frank,R., Leder,S., Joost,H.G. and Becker,W. (2000) Specificity determinants of substrate recognition by the protein kinase DYRK1A. *J. Biol. Chem.*, **275**, 2431–2438.
45. Schneider,P., Bayo-Fina,J.M., Singh,R., Kumar Dhanyamraju,P., Holz,P., Baier,A., Fendrich,V., Ramaswamy,A., Baumeister,S., Martinez,E.D., *et al.* (2015) Identification of a novel actin-dependent signal transducing module allows for the targeted degradation of GLI1. *Nat. Commun.*, **6**, 8023.
46. Park,J., Sung,J.Y., Park,J., Song,W.J., Chang,S. and Chung,K.C. (2012) Dyrk1A negatively regulates the actin cytoskeleton through threonine phosphorylation of N-WASP. *J. Cell Sci.*, **125**, 67–80.
47. Elagib,K.E., Brock,A., Clementelli,C.M., Mosoyan,G., Delehanty,L.L., Sahu,R.K., Pacheco-Benichou,A., Fruit,C., Besson,T., Morris,S.W., *et al.* (2022) Relieving DYRK1A repression of MKL1 confers an adult-like phenotype to human infantile megakaryocytes. *J. Clin. Invest.*, **132**, e154839.
48. Belin,B.J., Cimini,B.A., Blackburn,E.H. and Mullins,R.D. (2013) Visualization of actin filaments and monomers in somatic cell nuclei. *Mol. Biol. Cell*, **24**, 982–994.
49. Caridi,C.P., Plessner,M., Grosse,R. and Chiolo,I. (2019) Nuclear actin filaments in DNA repair dynamics. *Nat. Cell Biol.*, **21**, 1068–1077.
50. Scully,R., Panday,A., Elango,R. and Willis,N.A. (2019) DNA double-strand break repair-pathway choice in somatic mammalian cells. *Nat. Rev. Mol. Cell Biol.*, **20**, 698–714.
51. Wang,Y.H., Hariharan,A., Bastianello,G., Toyama,Y., Shivashankar,G.V., Foiani,M. and Sheetz,M.P. (2017) DNA damage causes rapid accumulation of phosphoinositides for ATR signaling. *Nat. Commun.*, **8**, 2118.
52. Sitar,T., Gallinger,J., Ducka,A.M., Ikonen,T.P., Wohlhoefler,M., Schmoller,K.M., Bausch,A.R., Joel,P., Trybus,K.M., Noegel,A.A., *et al.* (2016) Molecular architecture of the Spire-actin nucleus and its implication for actin filament assembly. *Proc. Nat. Acad. Sci. U.S.A.*, **108**, 19575–19580.
53. Murai,J., Huang,S.Y., Das,B.B., Renaud,A., Zhang,Y., Doroshow,J.H., Ji,J., Takeda,S. and Pommier,Y. (2012) Trapping of PARP1 and PARP2 by Clinical PARP Inhibitors. *Cancer Res.*, **72**, 5588–5599.
54. Mailand,N., Bekker-Jensen,S., Faustrup,H., Melander,F., Bartek,J., Lukas,C. and Lukas,J. (2007) RNF8 ubiquitylates histones at DNA double-strand breaks and promotes assembly of repair proteins. *Cell*, **131**, 887–900.
55. Tittel,J., Welz,T., Czogalla,A., Dietrich,S., Samol-Wolf,A., Schulte,M., Schwille,P., Weidemann,T. and Kerkhoff,E. (2015) Membrane targeting of the Spir·formin actin nucleator complex requires a sequential handshake of polar interactions. *J. Biol. Chem.*, **290**, 6428–6444.

---

**Received:** January 31, 2024. **Revised:** June 11, 2024. **Editorial Decision:** June 17, 2024. **Accepted:** June 20, 2024